Research in Astronomy and Astrophysics, 24:065010 (9pp), 2024 June https://doi.org/10.1088/1674-4527/ad3ec7
© 2024. National Astronomical Observatories, CAS and IOP Publishing Ltd. Printed in China and the U.K.

Probing the Kinematic Signatures of Planet Formation in the Gas Disk of MWC 480

Min Zhao[1], Haochuan Yu[2], and Zhengxiang Li[1]
[1] Department of Astronomy, Beijing Normal University, Beijing 100875, China; zxli918@bnu.edu.cn
[2] Sub-department of Astrophysics, Department of Physics, University of Oxford, Oxford, OX1 3RH, UK
Received 2024 February 6; revised 2024 March 24; accepted 2024 April 10; published 2024 May 22

Abstract

The disk around MWC 480 has shown multiple substructures in both dust and gas observations, possibly suggesting ongoing planet formation in situ. In this paper, we explore the gas kinematics of the MWC 480 disk by analyzing the archival Atacama Large Millimeter/submillimeter Array observations of ^{12}CO ($J = 2$-1), ^{13}CO ($J = 2$-1), and C^{18}O ($J = 2$-1). By modeling the line-of-sight velocities, inferred from the Doppler shifts of the emission lines, we are able to decompose the three-dimensional (3D) velocity field of the disk into rotational, radial, and vertical components. Further analysis reveals the presence of large-scale gas flows in the (r, z) plane. Notably, we identify potential meridional flows across various heights as traced by all three CO isotopologues in the 80–120 au region, possibly associated with ongoing planet formation activities in this region. Moreover, we find upward flows near 200 au for all three CO isotopologues, which may point to the presence of disk winds.

Key words: protoplanetary disks – planet-disk interactions – planet-star interactions

1. Introduction

Protoplanetary disks surrounding young stars are critical environments for planet formation. Studying these disks, especially the interactions between planets and disks is essential for understanding how planets form. Direct observation of planets forming within these disks is challenging, necessitating the use of indirect methods. In recent times, advancements in high-resolution observations, particularly in the submillimeter and near-infrared bands, have significantly improved our understanding of protoplanetary disks. These observations have revealed a wealth of substructures within these disks, such as rings, gaps, spirals, and cavities (e.g., ALMA Partnership et al. 2015; Isella et al. 2016; Andrews et al. 2018; Cieza et al. 2021). These substructures are believed to be indicative of the presence of protoplanets within the disks (e.g., Andrews 2020). Furthermore, the formation of embedded planets is expected to cause significant perturbations in the gas velocity structure of the disks. This aspect has been explored in various studies (e.g., Perez et al. 2015; Pérez et al. 2018; Pinte et al. 2018, 2019; Disk Dynamics Collaboration et al. 2020). In radio telescope data cube analysis, the extraction of velocity information is crucial because these cubes provide not only two-dimensional spatial projections but also a spectral axis. This spectral dimension, usually dominated by a single emission line, allows us to deduce the line-of-sight velocity by precisely locating the spectral line's central frequency. These new avenues have been opened thanks to the high spectral resolution capabilities of the Atacama Large Millimeter/submillimeter Array (ALMA).

Typically, the internal motions of the disk are dominated by the speed of rotation around the central star. The self-gravitation of the disk also affects the rotational velocity of the gas in the disk. However, considering the smooth and holistic influence of the disk's self-gravitation on the perturbations of rotational velocity, it will not generate perturbations at small scales (planet formation scale) in the disk (Rosenfeld et al. 2013). In this work our focus is not on the exact values of the rotational velocity but rather on its relative perturbations caused by planets within the disk. Therefore, following Teague et al. (2018a, 2018b, 2019, 2021) and Yu et al. (2021), in the context of a protoplanetary disk under the assumption of hydrostatic equilibrium and the neglect of self-gravitational effects, the rotational velocity ($v_{\rm rot}$) can be defined as (Rosenfeld et al. 2013)

$$\frac{v_{\rm rot}^2}{r} = \frac{GM_* r}{(r^2 + z^2)^{3/2}} + \frac{1}{\rho_{\rm gas}}\frac{\partial P}{\partial r}, \quad (1)$$

where M_* is the mass of the star, $\partial P/\partial r$ is the radial pressure gradient, $\rho_{\rm gas} = \mu_{\rm gas} n_{\rm gas}$ represents the gas volume density, and $\mu_{\rm gas}$ is the average molecular mass of the gas. For the ideal gas, $P = n_{\rm gas} kT$ represents the gas pressure. The embedded, forming planets in the protoplanetary disk can decrease the gas surface density in the region surrounding its orbital path, leading to large radial changes in the gas pressure gradient. Thus, embedded planets of sufficiently large mass can cause perturbations in the rotation velocity of the gas (Kanagawa et al. 2015; Teague et al. 2018a).

Moreover, the presence of embedded planets can induce radial ($v_{\rm rad}$) and vertical velocity (v_z). When there is a planet accreting gas in the protoplanetary disk, away from the midplane, the gas tends to refill the gap by viscous diffusion, producing meridional flow (e.g., Morbidelli et al. 2014; Szulágyi et al. 2014; Fung & Chiang 2016). Such meridional flows have been observed; Teague et al. (2019) detected the presence of meridional flows in the disk around HD 163296, and their location can be mapped to gaps in the millimeter continuum emission, suggesting that the presence of planets is the most likely scenario. In addition, Yu et al. (2021) detected meridional flows in the disk around HD 169142 in all three isotopologues of CO, which was the first investigation to track the coherent flow over a range of different heights in this disk, indicating an embedded planet.

The gas velocity observed using spectroscopy is the line-of-sight velocity, $v_{\rm LOS}$, which is theoretically composed of the system velocity $v_{\rm LSR}$ and the internal disk motions: the rotational velocity $v_{\rm rot}$, the radial velocity $v_{\rm rad}$, and the vertical velocity v_z. Its calculation formula is given by the equation (Pinte et al. 2023)

$$v_{\rm LOS} = v_{\rm LSR} + v_{\rm rot}\sin(|i|)\cos(\phi) + v_{\rm rad}\sin(i)\sin(\phi) - v_z\cos(i), \quad (2)$$

where i is the inclination of the disk, and ϕ is the azimuthal angle in the disk reference frame. Assuming the disk to be azimuthally symmetric, we can decompose its 3D velocity structures based on their distinct dependencies on ϕ. The orientation of the disk, and the decomposition of the line-of-sight velocity are illustrated in Figure 1.

MWC 480 is a 7-million-year-old Herbig Ae star located 161.8 pc away in the Taurus-Auriga star-forming region (Montesinos et al. 2009) and has a mass of 2.1 $M_\odot$ (solar mass) (Simon et al. 2019). Continuum observations suggest an inclination of 37° for the protoplanetary disk around MWC 480 (Huang et al. 2018). However, kinematic analysis suggests an inclination of 32.°4 is more consistent with their findings (Teague et al. 2021; Pinte et al. 2023). Previous studies have found abundant substructures in the MWC 480 dust continuum. For example, Long et al. (2018) found the disk is characterized by an inner disk encircled by a single ring. The location and shape of these components are modeled as symmetric Gaussian profiles. High-resolution ($0\farcs17 \times 0\farcs11$) ALMA Band 6 observations reveal a 23 au wide gap at 74.3 au and a ring at 97.5 au from the star (Liu et al. 2019). Further, Law et al. (2021) identified another gap at 149 au and a ring at 165 au, highlighting the disk's intricate structure. Molecular line emission observations also revealed rich substructures. The study of the ^{12}CO molecular line by Teague et al. (2021) has revealed vertical velocity perturbations centered at 245 au. They proposed that a planet located approximately 245 au from the star could be responsible for the observed perturbations. Izquierdo et al. (2023) employed an independent method to derive the rotational and vertical velocities of MWC 480 from Molecules with ALMA at Planet-forming Scales (MAPS) data for all three CO isotopologues, yielding results that corroborate those presented in Teague et al. (2021).

In this paper, we decompose the line of sight velocities of three CO isotopologues–^{12}CO ($J = 2-1$), ^{13}CO ($J = 2-1$), and C^{18}O ($J = 2-1$) into rotational, radial, and vertical components, yielding a comprehensive velocity profile of the MWC 480 disk. The structure of the paper is as follows: Section 2 summarizes the observational data and introduces the key observational properties of MWC 480. Section 3 describes the method of our data analysis. Section 4 shows our results, and Section 5 discusses the implications of the disk's velocity structure, focusing on its origins. Section 6 presents our conclusions and suggests directions for future research.

2. Target Selection and Spectroscopic Observations

We focused our study on the $J = 2$-1 rotational transitions of ^{12}CO, ^{13}CO and C^{18}O in the disk surrounding MWC 480. The data for this study were sourced from the ALMA Large Program—MAPS.[3] We refer readers to Czekala et al. (2021) for details of the observations and the data reductions. We utilized JvM-corrected images with robust = 0.5 weighting, achieving a synthesized beam of approximately $0\farcs17 \times 0\farcs12$ at a position angle (PA) of 6° for isotopologue emissions in MWC 480. All the images were generated with a 200 m s^{-1} channel spacing. The rms values of 0.73, 0.68, and 0.36 mJy per beam were determined for ^{12}CO ($J = 2-1$), ^{13}CO ($J = 2-1$), and C^{18}O ($J = 2-1$), respectively.

We calculated Moment 0 (velocity integrated intensity) maps for ^{12}CO ($J = 2-1$), ^{13}CO ($J = 2-1$), and C^{18}O ($J = 2-1$) using the `bettermoments`[4] (Teague & Foreman-Mackey 2018) package as shown in Figure 2. We also calculated the brightness temperature maps by measuring the peaks of the spectral lines and applying Planck's law to convert them to temperatures, see Figure 3.

To obtain the maps of the line of sight velocity v_0, we employed the "quadratic" method from the `bettermoments` (Teague & Foreman-Mackey 2018) package. This approach effectively calculates the line center of the line profile to get the line of sight velocity by identifying the pixel with the peak spectral intensity and two neighboring pixels on either side and fitting them with a quadratic function. We masked the resulting maps by masking regions where the peak intensity does not exceed five times the rms of a line-free channel, thereby excluding noise from the outer edges of the disk. This method provides a precise and detailed depiction of the spatial velocity distribution. The line-of-sight velocity maps for all three CO isotopologues are displayed in Figure 4.

[3] Data downloaded from: https://alma-maps.info/data.html

[4] Package downloaded from: https://github.com/richteague/bettermoments

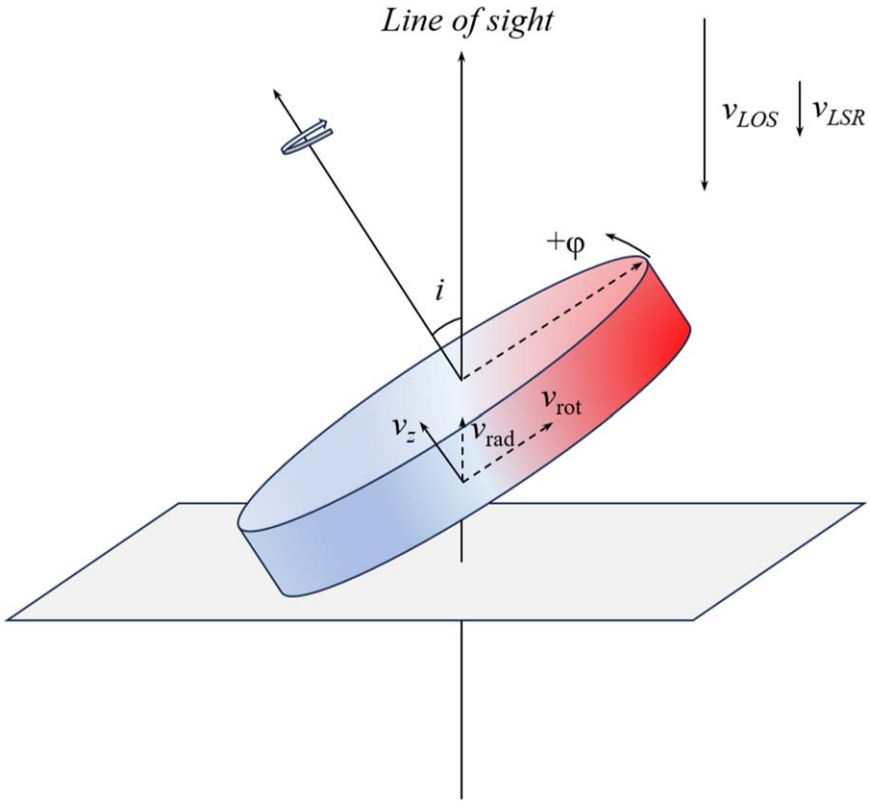

Figure 1. The schematic diagram of the orientation of the disk and the decomposition of the line-of-sight velocity. The line-of-sight direction is chosen vertically upward for ease of representation. The projection of $v_{\rm LOS}$ and $v_{\rm LSR}$ are in the opposite direction to the line-of-sight direction (the stellar system is moving away from us). The directions of $v_{\rm rot}$, $v_{\rm rad}$, and v_z in this figure represent the positive direction of velocity in the disk. The dashed line indicates the component is parallel to the disk midplane.

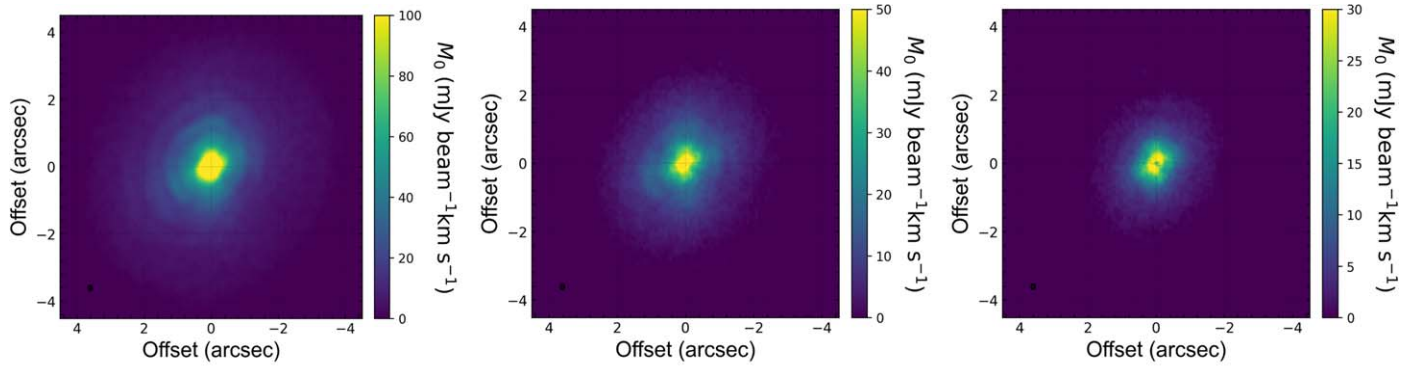

Figure 2. Moment zeroth maps of ^{12}CO ($J = 2 - 1$), ^{13}CO ($J = 2 - 1$), and C^{18}O ($J = 2 - 1$).

3. Method

To accurately measure 3D velocities, we need geometric information of the disk to project the data cube correctly and split it into annuli of constant radius. We fit the projected line-of-sight velocity $v_{\rm LOS}$ with a Keplerian velocity model and then we use the `eddy`[5] (Teague 2019) package to explore the posterior distributions of the model parameters. We fix the

[5] Package downloaded from: https://github.com/richteague/eddy

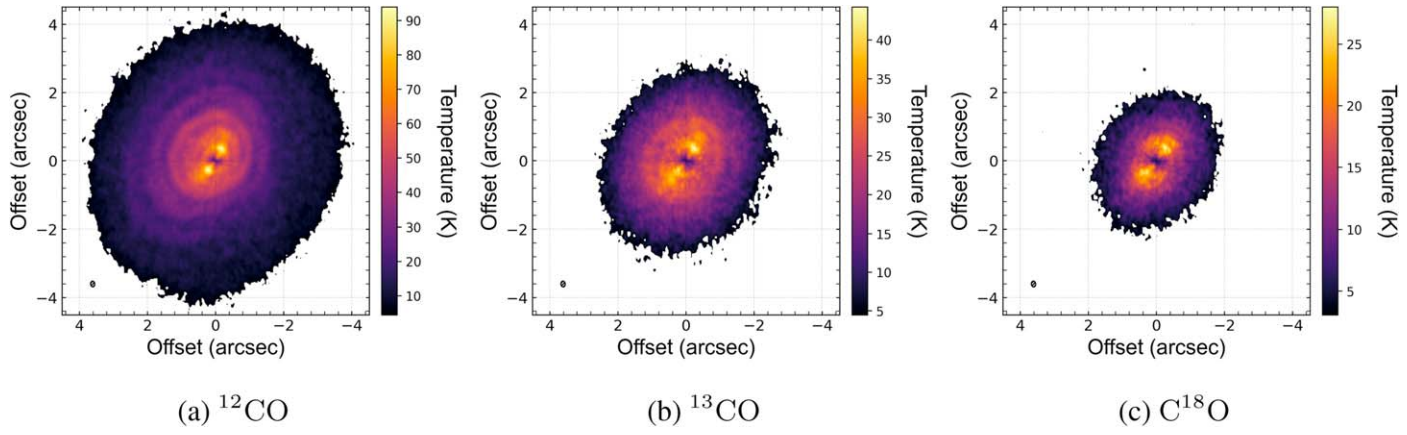

Figure 3. Brightness temperature maps of ^{12}CO ($J = 2 - 1$), ^{13}CO ($J = 2 - 1$), and C^{18}O ($J = 2 - 1$).

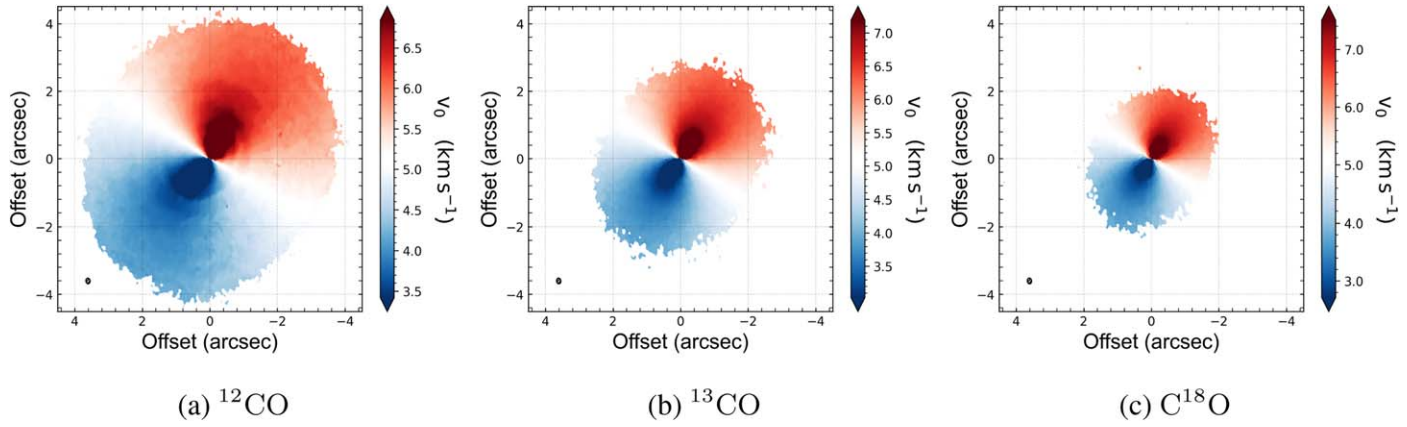

Figure 4. Line-of-sight velocity maps of ^{12}CO ($J = 2 - 1$), ^{13}CO ($J = 2 - 1$), and C^{18}O ($J = 2 - 1$).

inclination angle (i) of the disk and the parameters of the emission surface of each CO isotopologue. We take the same values with Teague et al. (2021) for these parameters. Specifically, the emission surface is described by a tapered power-law

$$z(r) = z_0 \times \left(\frac{r}{1''}\right)^{\psi} \times \exp\left(-\left[\frac{r}{r_{\rm taper}}\right]^{q_{\rm taper}}\right), \quad (3)$$

where $z(r)$ describes the height at a given radius r, ψ represents the power-law exponent, $r_{\rm taper}$ denotes the characteristic radius of the exponential taper, and $q_{\rm taper}$ is the exponent for the taper term.

The free parameters include the disk's image central position (Δx, Δy), PA, systemic velocity ($v_{\rm LSR}$) and the dynamical mass of the central star (M_*). We implemented a Markov Chain Monte Carlo (MCMC) approach using 64 walkers, 2000 burn-in steps, and 2000 steps to estimate posterior distributions of the free parameters in the model. The initial values of all parameters were referenced from Teague et al. (2021). Figure 5 shows the posterior distributions of the free parameters for all three CO isotopologues. Table 1 lists the best-fit values for each CO isotopologue. The values in the table are the median of the posterior distributions, and the statistical uncertainties are given by the 16th to 84th percentile range.

As shown in Equation (2), we can decompose the line-of-sight velocities $v_{\rm LOS}$ to the rotational, radial and vertical velocities, $v_{\rm rot}$, $v_{\rm rad}$, and $v_{\rm z}$, respectively. Given the predominantly azimuthal symmetry of the protoplanetary disk, it is reasonable to postulate that the first order $v_{\rm rot}$, $v_{\rm rad}$, and $v_{\rm z}$ maintain constant values at a certain radius. Note that, due to projection effects, the velocity line centers may exhibit variation across different azimuthal angles at a given radius, but such variations are negligible for the first-order approximation.

We used the `GoFish`[6] (Teague 2019) package to decompose the rotational and radial velocities. The disk was divided

[6] Package downloaded from: https://github.com/richteague/gofish

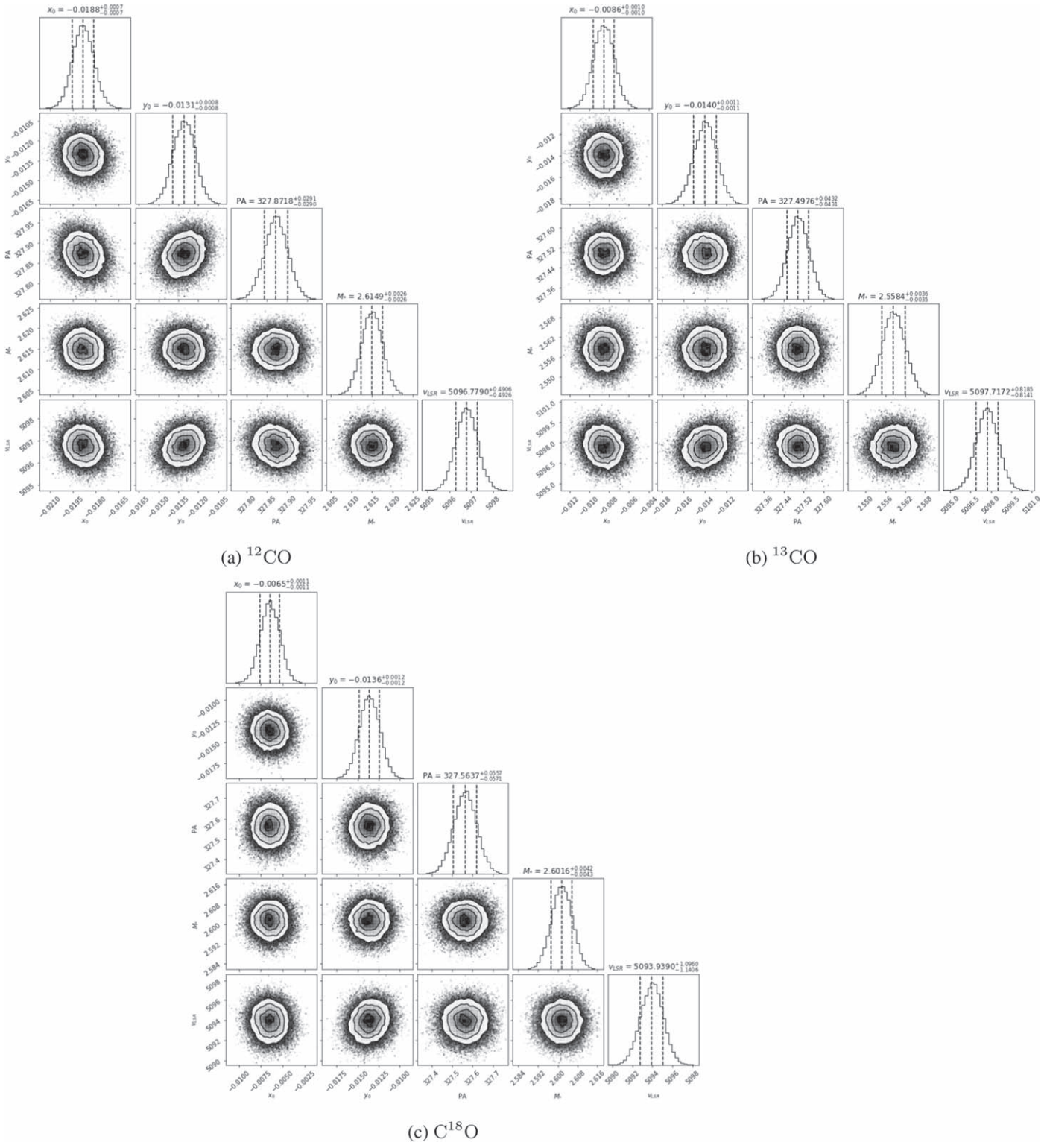

(a) ^{12}CO (b) ^{13}CO

(c) C^{18}O

Figure 5. The posterior distribution of the free parameters of the disk obtained by fitting the observed data of ^{12}CO ($J = 2 - 1$), ^{13}CO ($J = 2 - 1$), and C^{18}O ($J = 2 - 1$).

Table 1
Best-fit Values for Parameters Fitted with the Keplerian Model

Model Parameter	^{12}CO(2 − 1)	^{13}CO(2 − 1)	C^{18}O(2 − 1)
Δx_0 (mas)	-19 ± 1	-9 ± 1	-7 ± 1
Δy_0 (mas)	-13 ± 1	-14 ± 1	-14 ± 1
i (°)	[−32.4]	[−32.4]	[−32.4]
PA (°)	327.9 ± 0.1	327.5 ± 0.1	327.6 ± 0.1
M_* ($M_\odot$)	2.61 ± 0.01	2.56 ± 0.01	2.60 ± 0.01
$v_{\rm LSR}$ (km s^{-1})	5.10 ± 0.01	5.10 ± 0.01	5.09 ± 0.01
z_0 ($''$)	[0.30]	[0.11]	[0.07]
ψ (−)	[1.32]	[1.17]	[1.18]
$r_{\rm taper}$ ($''$)	[3.27]	[1.43]	[1.09]
$q_{\rm taper}$ (−)	[2.73]	[4.11]	[3.11]
d (pc)	[161.8]	[161.8]	[161.8]

Note. The values shown are the median of the posterior distribution, with uncertainty given by the 16th–84th percentile range. The values in brackets remain constant during the fitting process.

into concentric annuli, each with a width equal to one-fourth of the beam's major FWHM. A random set of spatially independent pixels was selected for velocity extraction within these annular sections. We utilized the Gaussian process method to extract the rotation and radial velocities at each annulus. We could derive the rotational ($v_{\rm rot}$) and radial ($v_{\rm rad}$) velocities from Equation (2), owing to their distinct dependencies on the azimuth angle. The best-fit $v_{\rm rot}$ and $v_{\rm rad}$ values are defined as those that best align the individual spectra, quantified by the difference between a smooth Gaussian process model and the stacked spectrum. The main advantage of this approach is that it does not require any assumptions about the exact shapes of the underlying spectral profiles. We refer readers to Teague et al. (2018b) for details. The whole process was repeated 20 times for each annulus, randomly selecting new pixels to minimize features in the radial profile that could be attributed to noisy pixels (e.g., Keppler et al. 2019). According to Equation (2), the value of $v_{\rm rad}$ being positive means that the direction of $v_{\rm rad}$ is toward the central star. Therefore, following Teague et al. (2019), after extracting $v_{\rm rad}$, we apply a negative sign to it to ensure that a positive $v_{\rm rad}$ represents motion away from the star.

To decompose the vertical velocity, we rely on the fact that the vertical velocity component, v_z, does not vary with the azimuthal angle ϕ, as indicated by Equation (2). Hence, the process is independent of the decomposition of the rotational and radial velocities mentioned above. Following the method described by Yu et al. (2021), we extracted the v_z profiles by subtracting the projected rotational and radial velocities, as well as $v_{\rm LSR}$, from the v_0 map.

4. Result

The 3D velocity profiles obtained from our analysis are presented in Figure 6. The first row depicts the rotational velocity ($v_{\rm rot}$), while the second row illustrates its perturbations ($\delta v_{\rm rot}$). The radial ($v_{\rm rad}$) and vertical velocity profiles ($v_{\rm z}$) are displayed in the third and fourth rows respectively. The shaded areas in each panel represent the uncertainties associated with these velocity profiles. The blue vertical dashed lines in the lower three rows represent the center of the gaps in the dust continuum observation. This kinematic technique is only effective at distances more than twice the beam's long-axis radius from the center (Teague et al. 2018a), thus, the minimum radius applicable for fitting all our velocity profiles is set at about 50 au.

To obtain the rotational velocity perturbations $\delta v_{\rm rot}$, following Teague et al. (2019), we used a tenth-order polynomial to fit a smooth rotational velocity background model after getting $v_{\rm rot}$. This method is effective in fitting the baseline of rotational velocity by not assuming any specific physical mechanisms for the disk's rotational velocity. It effectively integrates all significant, larger-scale structures into the background model, thereby isolating only those perturbations (reflected in higher-order terms) relevant to scales of planetary formation. Then, we used the Butterworth low-pass filter with a cut-off of six samples (∼40 au) and an order 3 to obtain perturbations corresponding to the spatial scale of planet formation. Our analysis reveals the rotational velocities within the protoplanetary disk, as indicated by CO isotopologue emissions (^{12}CO, ^{13}CO, and C^{18}O), deviate from the Keplerian motion. As shown in the panels of the second row in Figure 6, the velocity perturbations ($\delta v_{\rm rot}$) for all isotopologues share a similar trend of alternating positive and negative velocities up to a radial distance of 240 au, with ^{13}CO displaying the slightest perturbation speed. The purple arrows in the figure signify the minima of the local pressure, which relate to the potential planetary locations by Equation (1). The radial profile of $\delta v_{\rm rot}$, particularly the overall trends along the radius axis, is in good agreement with results presented in Teague et al. (2021) and Izquierdo et al. (2023).

Regarding radial velocity, we find uniformity across all three CO isotopologues up to a distance of 130 au. After that the structure of C^{18}O was almost submerged in uncertainty. Specifically, ^{12}CO exhibited a radial velocity as high as 90 m s^{-1} at 230 au. For vertical velocities, ^{12}CO shows a speed of 70 m s^{-1} at 230 au. ^{13}CO and C^{18}O are well consistent with each other in their vertical velocity profiles and are flatter than ^{12}CO, as shown in the panels of the fourth row in Figure 6. The vertical velocity structure of all three CO isotopologues is also consistent with the results from Izquierdo et al. (2023). Compared to ^{12}CO,^{13}CO and C^{18}O exhibit fewer vertical velocity substructures, but both show a vertical speed greater than 20 m s^{-1} at about 100 au.

In comparison with Izquierdo et al. (2023), we have not only decomposed the rotational and vertical velocities but also the radial velocity. This enables us to examine the gas flows in the edge-on orientation, i.e., in the (r, z) plane. As shown in

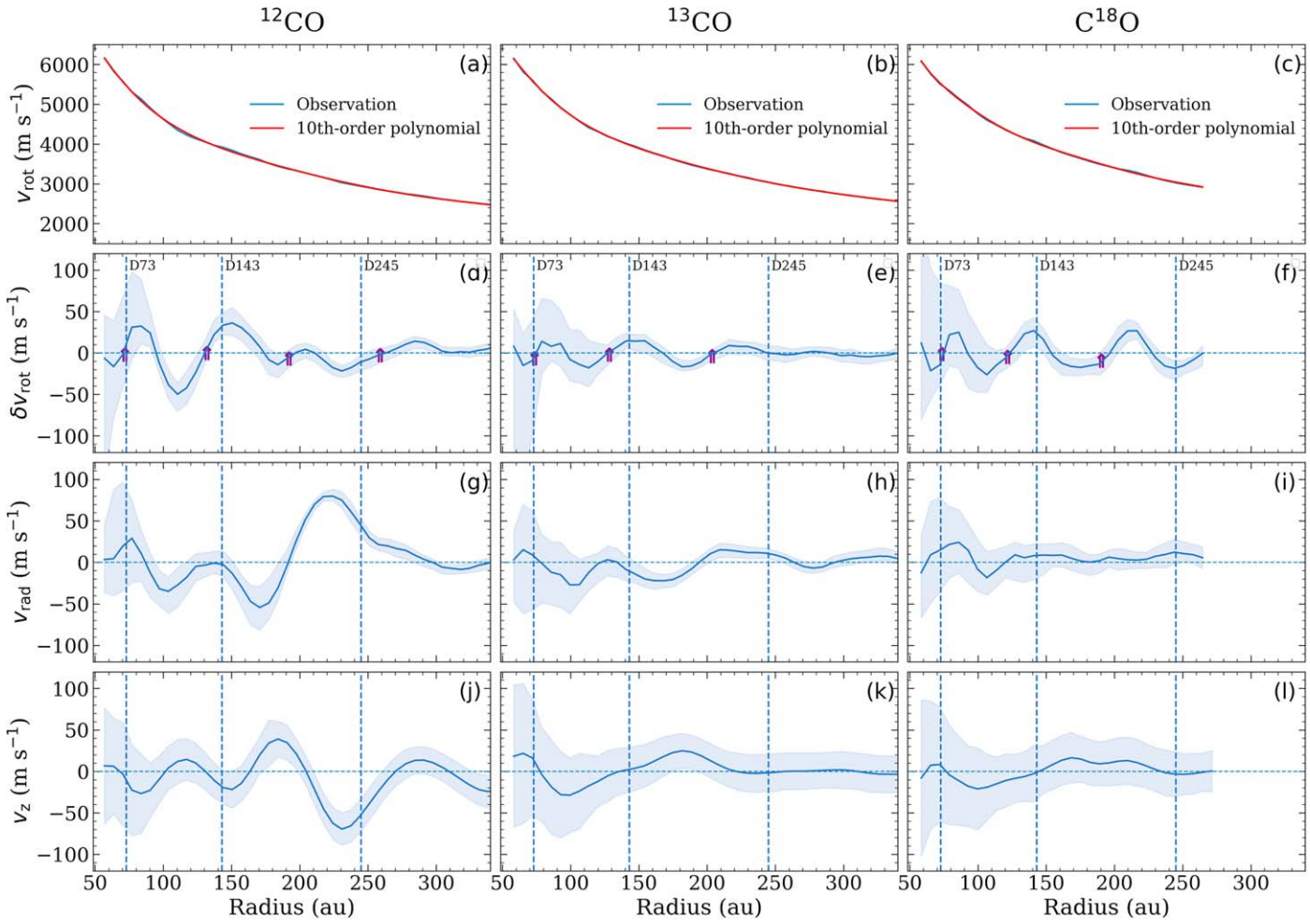

Figure 6. The velocity profiles for ^{12}CO ($J = 2 - 1$), ^{13}CO ($J = 2 - 1$), and C^{18}O ($J = 2 - 1$) are shown in the left, middle, and right columns, respectively. Panels in the top row depict the rotational velocity ($v_{\rm rot}$), while those in the second row illustrate perturbations in the rotational velocity ($\delta v_{\rm rot}$). Subplots in the third row show the radial velocity ($v_{\rm rad}$) and those in the fourth row visualize the vertical velocity (v_z). Shaded areas in each plot represent uncertainties in the velocity profiles.

Figure 7, the starting points of the arrows represent the positions of the gas emission surfaces, which is defined by Equation (3), with the values of each parameter presented in Table 1. Each CO isotopologue marks different layers within the disk, with ^{12}CO being closer to the disk surface and C^{18}O closer to the midplane. The results show that between 80 and 120 au, all three CO isotopologues exhibit coherent collapsing flows indicated by the black dotted box in the figure. Gas near these regions converges and descends toward the disk's midplane. Remarkably, this is the first observation of coherent collapsing flows across multiple altitudes within this disk. Such flows could be described by the meridional flows actuated by a planet predicted by theoretical models. We interpret and discuss these flows in Section 5. Between 160 and 220 au, all three isotopologues show coherent upward flows, which might be attributed to disk winds (e.g., Galloway-Sprietsma et al. 2023).

5. Discussion

Figure 7 reveals the presence of a coherent collapsing gas flow at approximately 100 au, indicated by a black dotted box. Similar flows have also been observed in HD 163296 (Teague et al. 2019) and HD 169142 (Yu et al. 2021). These flows could possibly be explained by meridional flows that are linked to the decrease of gas surface density, which is caused by planet-disk interactions. This suggests the possibility of a planet-induced gap at approximately 100 au. Away from the midplane, the gas tends to fill into the gap by viscous diffusion because it is not sufficiently repelled by the planetary torque. Upon entering the gap, the gas falls toward the midplane to restore hydrostatic equilibrium, inducing a meridional flow from the disk's surface to its midplane. (e.g., Papaloizou & Lin 1984; Kley et al. 2001; Morbidelli et al. 2014; Szulágyi et al. 2014). Nonetheless, alternative mechanisms, such as magnetorotational instability

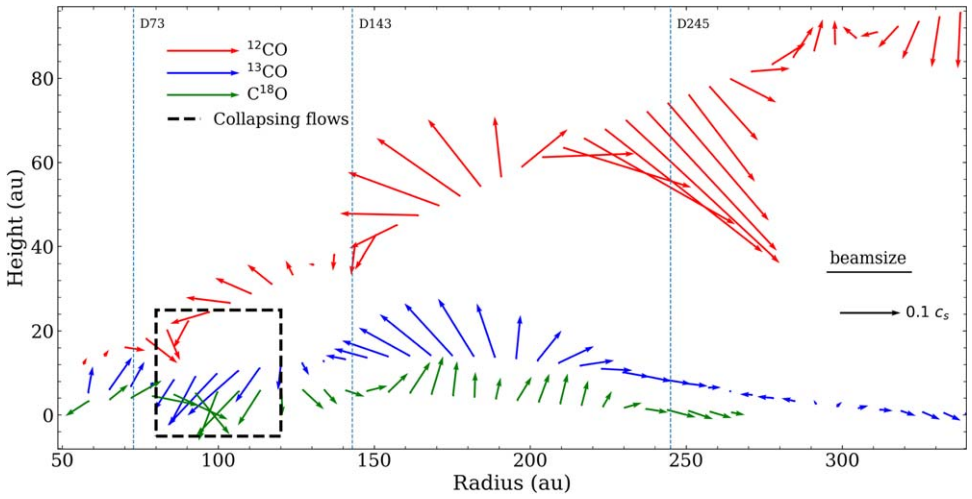

Figure 7. Gas flows in the (r, z) plane of all three CO isotopologues. The highlighted black dashed box is a region of coherent gas collapse, approximately at around 100 au. For reference, a vector in the bottom right corner represents 0.1 c_s.

and vertical shear instability (Flock et al. 2015, 2017; Riols & Lesur 2019), might also lead to collapsing flows. Comprehensive simulation is essential to ascertain the definitive origins of such dynamic flows.

According to our findings, the location of the potential meridional flows that we have identified corresponds with the falling edge of the radial profile of $\delta v_{\rm rot}$, as shown in the second row of Figure 6. This suggests an increase in the gas molecular volume density at these locations, as depicted by Equation (1). According to the full thermochemical models in Rab et al. (2020) and the simplified model used in Yu et al. (2021), there is a non-trivial response of number density to the variations in the surface density. As a result, despite the increase in gas volume density, a decrease in gas surface density may occur. For instance, the study by Yu et al. (2021) indicates that the gas kinematic structure at 125 au, characterized by an increased gas volume density, aligns with the models of a moderate depth gap, i.e., with surface density depletion (δ) between 0.07 and 0.003. This suggests that at this location, the CO emission may probe deeper into the disk (i.e., lower $z_{\rm CO}$), encountering gas that is hotter and denser (i.e., higher temperature and molecular volume density).

Similarly, in this work, the inferred structure at around $r = 100$ au necessitates a gas surface density minimum based on the potential meridional flows in this region, accompanied by an increased gas volume density as indicated by $\delta v_{\rm rot}$. This is consistent in all three CO isotopologues, suggesting a gap potentially carved by a planet at approximately 100 au. A more detailed discussion can follow the model proposed by Yu et al. (2021), which allows for the derivation of a range of values for surface density depletion and then enables us to estimate the mass of the potential planet present at that location through further studies.

6. Conclusion

In this work, to unveil the overarching kinematic signatures of the MWC 480 disk, we have analyzed the ^{12}CO ($J = 2 - 1$), ^{13}CO ($J = 2 - 1$), and C^{18}O ($J = 2 - 1$) emission lines from the observations in the MAPS program. We employed the method developed by Teague et al. (2018b, 2019), and successfully extracted the 3D velocity structures for different emission layers within the disk, each demarcated by the different CO isotopologues. Our investigation unveils extensive (r, z) plane flows, with collapsing flows observed across all three isotopologue layers between 80 and 120 au which suggests the potential presence of planets in this region–a prospect that merits further exploration. Additionally, the upward flows detected near 200 au may indicate disk winds. To enhance our understanding of these phenomena, engaging in more comprehensive modeling and numerical simulations essential for achieving more definitive findings is imperative.

Acknowledgments

This work was supported by the National Key Research and Development Program of China grant No. 2021YFC2203001; National Natural Science Foundation of China (NSFC, Grant Nos. 12322301 and 12275021); the Strategic Priority Research Program of the Chinese Academy of Sciences, grant No. XDB2300000 and the Interdiscipline Research Funds of Beijing Normal University.

References

ALMA Partnership, Brogan, C. L., Pérez, L. M., et al. 2015, ApJL, 808, L3
Andrews, S. M. 2020, ARA&A, 58, 483
Andrews, S. M., Huang, J., Pérez, L. M., et al. 2018, ApJL, 869, L41

Cieza, L. A., González-Ruilova, C., Hales, A. S., et al. 2021, MNRAS, 501, 2934
Czekala, I., Loomis, R. A., Teague, R., et al. 2021, ApJS, 257, 2
Disk Dynamics Collaboration, Armitage, P. J., Bae, P. J., et al. 2020, arXiv:2009.04345
Flock, M., Fromang, S., Turner, N. J., & Benisty, M. 2017, ApJ, 835, 230
Flock, M., Ruge, J. P., Dzyurkevich, N., et al. 2015, A&A, 574, A68
Fung, J., & Chiang, E. 2016, ApJ, 832, 105
Galloway-Sprietsma, M., Bae, J., Teague, R., et al. 2023, ApJ, 950, 147
Huang, J., Andrews, S. M., Dullemond, C. P., et al. 2018, ApJL, 869, L42
Isella, A., Guidi, G., Testi, L., et al. 2016, PhRvL, 117, 251101
Izquierdo, A. F., Testi, L., Facchini, S., et al. 2023, A&A, 674, A113
Kanagawa, K. D., Tanaka, H., Muto, T., Tanigawa, T., & Takeuchi, T. 2015, MNRAS, 448, 994
Keppler, M., Teague, R., Bae, J., et al. 2019, A&A, 625, A118
Kley, W., D'Angelo, G., & Henning, T. 2001, ApJ, 547, 457
Law, C. J., Loomis, R. A., Teague, R., et al. 2021, ApJS, 257, 3
Liu, Y., Dipierro, G., Ragusa, E., et al. 2019, A&A, 622, A75
Long, F., Pinilla, P., Herczeg, G. J., et al. 2018, ApJ, 869, 17
Montesinos, B., Eiroa, C., Mora, A., & Merín, B. 2009, A&A, 495, 901
Morbidelli, A., Szulágyi, J., Crida, A., et al. 2014, Icarus, 232, 266
Papaloizou, J., & Lin, D. N. C. 1984, ApJ, 285, 818
Pérez, S., Casassus, S., & Benítez-Llambay, P. 2018, MNRAS, 480, L12
Perez, S., Dunhill, A., Casassus, S., et al. 2015, ApJL, 811, L5
Pinte, C., Price, D. J., Ménard, F., et al. 2018, ApJL, 860, L13
Pinte, C., Teague, R., Flaherty, K., et al. 2023, in ASP Conf. Ser. 534, Protostars and Planets VII, ed. S. Inutsuka et al. (San Francisco, CA: ASP), 645
Pinte, C., van der Plas, G., Ménard, F., et al. 2019, NatAs, 3, 1109
Rab, C., Kamp, I., Dominik, C., et al. 2020, A&A, 642, A165
Riols, A., & Lesur, G. 2019, A&A, 625, A108
Rosenfeld, K. A., Andrews, S. M., Hughes, A. M., Wilner, D. J., & Qi, C. 2013, ApJ, 774, 16
Simon, M., Guilloteau, S., Beck, T. L., et al. 2019, ApJ, 884, 42
Szulágyi, J., Morbidelli, A., Crida, A., & Masset, F. 2014, ApJ, 782, 65
Teague, R. 2019, JOSS, 4, 1632
Teague, R. 2019, JOSS, 4, 1220
Teague, R., Bae, J., Aikawa, Y., et al. 2021, ApJS, 257, 18
Teague, R., Bae, J., Bergin, E. A., Birnstiel, T., & Foreman-Mackey, D. 2018a, ApJL, 860, L12
Teague, R., Bae, J., Birnstiel, T., & Bergin, E. A. 2018b, ApJ, 868, 113
Teague, R., Bae, J., & Bergin, E. A. 2019, Natur, 574, 378
Teague, R., & Foreman-Mackey, D. 2018, RNAAS, 2, 173
Yu, H., Teague, R., Bae, J., & Öberg, K. 2021, ApJL, 920, L33